Nanoscale Imaging of Mineral Crystals inside Biological Composite Materials Using X-Ray Diffraction Microscopy

Huaidong Jiang,[1] Damien Ramunno-Johnson,[1] Changyong Song,[1] Bagrat Amirbekian,[1] Yoshiki Kohmura,[2]
Yoshinori Nishino,[2] Yukio Takahashi,[3] Tetsuya Ishikawa,[2] and Jianwei Miao[1,*]
[1]*Department of Physics and Astronomy, University of California, Los Angeles, California 90095, USA*
[2]*RIKEN SPring-8 Center, 1-1-1, Kouto, Sayo, Hyogo 679-5148, Japan*
[3]*Graduate School of Engineering, Osaka University, Osaka 565-0871, Japan*
(Received 2 May 2007; published 24 January 2008)

We for the first time applied x-ray diffraction microscopy to the imaging of mineral crystals inside biological composite materials—intramuscular fish bone—at the nanometer scale resolution. We identified mineral crystals in collagen fibrils at different stages of mineralization. Based on the experimental results and biomineralization analyses, we suggested a dynamic model to account for the nucleation and growth of mineral crystals in the collagen matrix. The results obtained from this study not only further our understanding of the complex structure of bone, but also demonstrate that x-ray diffraction microscopy will become an important tool to study biological materials.

DOI: 10.1103/PhysRevLett.100.038103 PACS numbers: 87.57.N−, 61.05.cp, 87.85.J−

Because x rays have a longer penetration depth than electrons and destructive sample preparation is often avoidable, x-ray scattering has been widely used in the analysis of biological structures such as bone [1,2], muscles [3,4], protein and RNA foldings [5], and lipid-DNA complexes [6]. While conventional x-ray scattering methods can probe structures on a subnanometer length scale, they usually provide globally averaged information and a preassumed model is often required to fit the experimental data. By using coherent x rays from 3rd generation synchrotron radiation sources, x-ray diffraction microcopy (or lensless imaging) has been developed to imaging noncrystalline specimens at the nanometer scale resolution [7–13], in which x-ray diffraction patterns are directly inverted to high-resolution images by the oversampling iterative method [14]. In this Letter, we applied x-ray diffraction microscopy to the imaging of the mineral crystals inside biological composite materials—intramuscular bone—at different stages of mineralization.

The mechanical and physiological functions of bone as an organ, tissue, and substance are highly dependent on the structural, spatial, and chemical interactions of its major components: the mineral phase, the collagen fibrils, and the noncollagenous proteins [15]. Previous studies have indicated hierarchical and highly ordered structures in bone based on small-angle x-ray and neutron scattering [1,16], TEM [15], and atomic force microscopy [17]. Subsequently, 2D and 3D models of the supramolecular structure of collagen fibrils have been developed to demonstrate the remarkable architecture [18]. Despite these studies, however, the exact relationships between mineral crystals and collagen fibrils at the ultrastructural and molecular levels continue to be a major scientific challenge [15]. An important aspect of this challenge is to understand the dynamic structure of mineral phase in bone at different stages of mineralization, which is of fundamental importance in biology and medicine.

Here we studied intramuscular fish bone from Alewife herring, having a different content of mineral crystals. This material is composed mostly of collagen and other proteins with a calcium phosphate (apatite) mineral phase embedded inside the collagen fibrils [19]. Bones were freshly dissected, frozen, and ground as previously described [19]. Prior to grinding, the bones were divided into sections of no, low, and high mineral crystal contents. Bone particles with a size of ~2 μm were dispersed in pure ethanol and deposited on thin silicon nitride membranes. The well-isolated and micron-sized particles were selected by a light microscope and used for the coherent x-ray diffraction experiment.

The diffraction microscope, shown in Fig. 1, was mounted on an undulator beam line (BL29XUL) at SPring-8 [20], which provides 5 keV monochromatic x rays. A 20-μm pinhole was placed in front of the sample to make a small and coherent beam. The pinhole produced an Airy pattern as well as the parasitic scattering due to the surface roughness of the pinhole edge. A silicon aperture with beveled edges, positioned just in front of the sample, was used to clean the parasitic scattering and the higher orders of the Airy pattern. The sample was mounted on a rotary stage for 3D data acquisition. The diffraction patterns were collected by a liquid-nitrogen-cooled CCD detector. The distance between the sample and the detector was adjustable so that the missing data due to a beam stop were confined within the centro-speckle [21]. To eliminate scattering from air and operate the CCD in liquid nitrogen temperatures, the experiment was performed in vacuum with a pressure of ~10^{-6} torr. By using this microscope, coherent x-ray diffraction patterns were obtained from bone particles at different stages of mineralization.

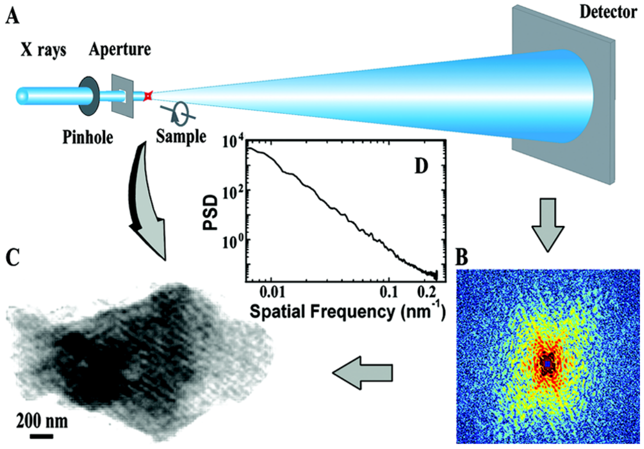

FIG. 1 (color online). (a) Schematic diagram of the x-ray diffraction microscope. (b) Diffraction pattern of a highly mineralized bone particle. (c) Reconstructed image from (b). (d) Power spectral density of the diffraction pattern, indicating a resolution of 24 nm (i.e., a pixel size of 12 nm).

Figures 1(b) and 1(c) show the diffraction pattern and the corresponding reconstructed image of a highly mineralized bone particle. The exposure time of the diffraction pattern is 120 minutes. The power spectrum density of Fig. 1(b) is shown in Fig. 1(d), indicating a pixel size of 12 nm.

The phase retrieval of the diffraction patterns was carried out by using the guided hybrid input and output algorithm (GHIO) [22,23]. The GHIO algorithm began with 16 independent reconstructions on each diffraction pattern with random phases as the initial input. Each reconstruction was iterated back and forth between real and reciprocal space. In real space the electron density outside a support and the negative density inside the support were pushed close to zero where the support represents a boundary somewhat larger than the sample envelope. In reciprocal space the Fourier modulus remained unchanged, while the phases were updated in each iteration. After 2000 iterations, we obtained 16 images (ρ^i_{old}), defined as the 0th generation. An R_F was calculated for each of the 16 images $R_F = \sum ||F_{\text{exp}}| - \alpha|F_{\text{cal}}||/\sum |F_{\text{exp}}|$, where $|F_{\text{exp}}|$ and $|F_{\text{cal}}|$ represent the experimental and calculated Fourier modulus, and α the scaling factor. The image with the smallest R_F was chosen as a seed (ρ_{seed}). A set of new images (ρ^i_{new}) was obtained by $\rho^i_{\text{new}} = \sqrt{\rho_{\text{seed}}\rho^i_{\text{old}}}$, where $i = 1, 2, \ldots, 16$. The new 16 images were used as the initial inputs for the next generation. This step merged the best image in the current generation with each of the 16 images so that the “favorable gene” (i.e., the smallest R_F) would be passed on to the succeeding generations. We repeated the procedures for each generation and, after 9 generations, the 16 images became consistent and the one with the smallest R_F was chosen as the final image. By using the GHIO algorithm, we inverted each coherent x-ray diffraction pattern to an image.

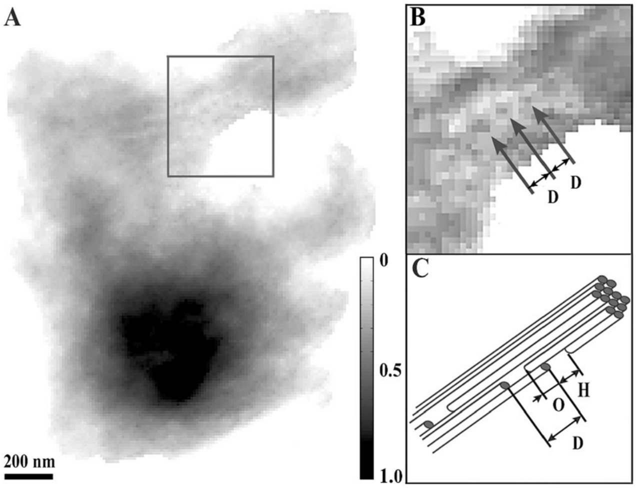

FIG. 2. (a) Reconstructed image of unmineralized bone. (b) The zoom-in image indicates that the period of the small island dark spots along the fibril direction (indicated by the arrows) is ~67 nm. (c) Staggered arrangement of collagen molecules. Collagen molecules with ~300 nm long and 1.5 nm in diameter are staggered to each other by D (~67 nm), which includes an overlap region O (~27 nm) and a hole region H (~40 nm).

Figure 2(a) shows the reconstructed image of unmineralized collagen fibrils. The gray scale in the image represents the variation of the electron density. The periodicity of dark spots [indicated by the arrows in Fig. 2(b)] along the fibril direction is ~67 nm, which is consistent with the small-angle x-ray scattering results from the same bone samples [16]. The 67 nm periodicity directly confirms the staggered arrangement of collagen molecules [Fig. 2(c)], which is based on the 2D Hodge model [18].

Figure 3(a) shows the reconstructed image from low mineralization bone. The reconstructed image indicates that the mineralized collagen fibrils are somewhat parallel to each other. The lineout across the individual collagen fibrils is shown in Fig. 3(b) (right). The distance between the two neighboring fibrils was estimated to be ~50–60 nm. Because the mineral crystals deposited in the collagen fibrils possess high electron density, the collagen fibrils are more easily to be identified than unmineralized collagen fibrils (Fig. 2). Figure 3(b) (left) shows that the dense mineral crystals (indicated by the arrows) are nonuniformly deposited in the collagen fibrils with periodicity of ~67 nm, which corresponds to the repeat of the collagen hole regions [Fig. 2(c)]. This observation verifies that the mineral crystals, used to strengthen the collagen fibrils, are initially deposited in the hole regions.

Figures 3(c) and 3(d) show the reconstructed images of the same low mineralization bone at −45° and +45°, respectively. In comparison with the image at 0° [Fig. 3(a)], the collagen fibrils are no longer visible after rotation of the sample. In addition, there are dark spots or domains spreading out in the images which are likely due to the mineral crystals deposited in the fibrils and the thickness variation of the sample. The images shown in Fig. 3 imply that mineral crystals nucleate and grow in the

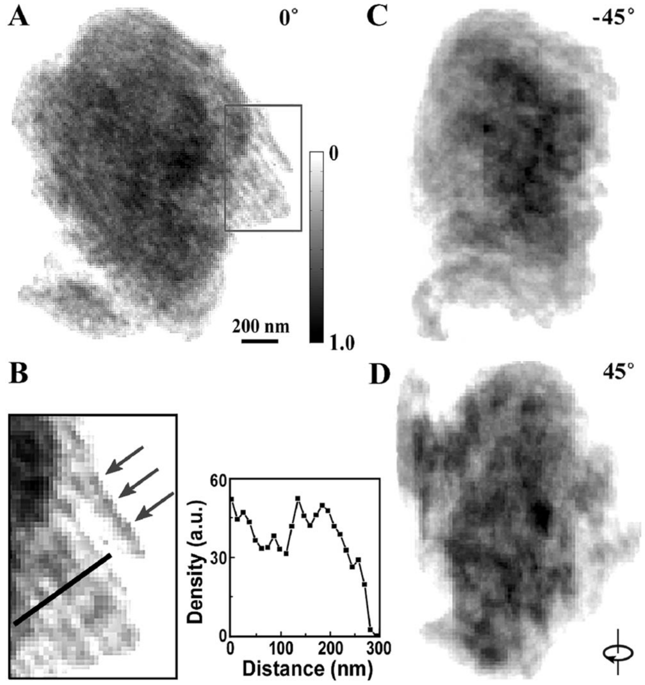

FIG. 3. Reconstructed images of a low mineralized bone particle. (a) The image at 0° reveals the mineralized collagen fibrils are highly aligned. (b) Zoom-in view of the rectangular area (left) and lineout across the individual collagen fibrils (right). The period of dark spots (arrows) is ~67 nm. (c), (d) Reconstructed images of the same low mineralized bone particle at $-45°$ and $+45°$, respectively.

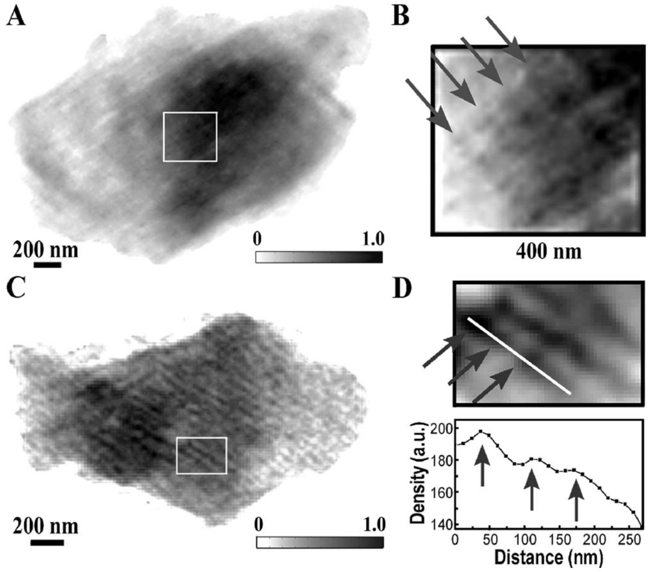

FIG. 4. (a) Reconstructed image of a highly mineralized bone particle. (b) Zoom-in view of the white square region shows a band structure (indicated by the arrows) with a period of ~67 nm. (c) Reconstructed image of another highly mineralized fish bone particle. (d) Zoom-in view of the rectangular region and the lineout along the fibril direction indicate the high-density hole regions has a periodicity of ~67 nm.

hole regions, and the distribution of deposited crystals is nonuniform.

Figure 4(a) shows the reconstructed image of a highly mineralized bone particle. The zoom-in view [Fig. 4(b)] indicates that dense mineral crystals fill up the hole regions and form a band structure with periodicity of ~67 nm as indicated by the arrows. Figure 4(c) shows the reconstructed image of another highly mineralized bone particle. The mineralized fibrils are almost parallel to each other and also vary periodically in density along the fibril axis. The zoom-in view [Fig. 4(d)] and the lineout along the fibril direction show a period of ~67 nm within the fibril. In the latest stage of mineralization, the mineral crystals deposited beyond the hole regions form fully calcified collagen fibrils. The excess mineral crystals eventually fill up the small spaces between the collagen molecules and cause the band structure to broaden or even disappear in some regions.

Based on the results of the x-ray diffraction microscope and our biomineralization analyses [24], we suggested a dynamic model to account for the nucleation and growth of mineral crystals in collagen matrix, which improves upon the previously proposed model of bone mineralization (reviewed in [15]) by taking into account structure characteristics of collagen, kinetics of crystal nucleation and growth, the relationship between collagen fibrils and crystals, and stages of bone maturation. Body fluid existing in the hole regions and the small space between adjacent collagen molecules provides supersaturation for nucleation and growth of mineral crystals [Fig. 5(a)]. Because of relatively larger space and better diffusion, body fluid in the holes provides relatively stable supersaturation and continuous growth units in early mineralization. Furthermore, collagen molecules serve as the nucleation sites and lower the nucleation barrier, which promotes oriented nucleation of mineral crystals [25,26]. Consequently, most mineral crystals are initially deposited in the hole regions via heterogeneous nucleation and growth with the *C* axis parallel to the longitudinal fibril axis [Fig. 5(b)], which leads to strong and tough biomaterials. A recent molecular model of nascent bone formation also indicates the characteristic nanostructure is vital for its high strength and its

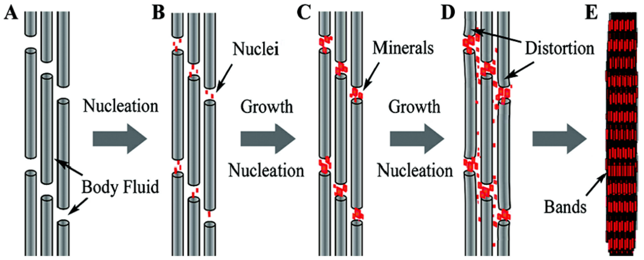

FIG. 5 (color online). Schematic illustration of the suggested dynamic mechanism for the nucleation, growth, and orientation of mineral crystals in the collagen matrix at different stages of mineralization.

ability to sustain large deformation, which is relevant to the physiological role of bone [27].

The existing mineral crystals will further induce self-epitaxial nucleation and growth in the hole regions. The self-epitaxial nucleation at proper conditions results in well-ordered and parallel crystals in local regions [25]. With maturation of bone, more and more mineral crystals nucleate and grow in the hole regions within the collagen matrix. These crystals deposited in the hole regions produce periodic density distributions along the longitudinal fibril axis [i.e., band structure in Fig. 5(e)]. This ordered and compact nanostructure of mineralized collagen fibrils significantly improves the mechanical properties of bone and increases the resistance to fracture [27].

In the final stage of mineralization, there is not enough hole space to house the mineral crystals. Further mineralization of the collagen fibrils is hence propagated in the space between collagen molecules, and eventually fills up all of the available space. Because of limited space, bad diffusion between the collagen molecules, and unstable supersaturation, mineral crystals formed in the collagen space are usually smaller than those in the hole regions [Fig. 5(d)]. Consequently, the axial period of the mineral phase in fibrils becomes a little obscure due to the deposition of crystals throughout the available spaces including the collagen space. This would definitely change the structure of collagen framework by converting the soft pliable fibrils into a continuous hard substance. Our experimental results have indeed indicated that there is expansion of the collagen fibrils around the hole regions, which permits the deposition of additional crystals [Figs. 4(c) and 4(d)]. In addition, further deposition of minerals probably causes considerable distortion of the fibrils, which results in poor mechanical properties of bone since the stress will not be properly redistributed between mineral crystals and the collagen matrix [28].

In summary, we have performed 3D spatial analysis of the mineral crystals inside the collagen matrix by using x-ray diffraction microscopy. We identified the spatial relationship of mineral crystals to collagen matrix at different stages of mineralization. Based on the experimental results and our biomineralization analyses, we suggested a dynamic model to account for the nucleation, growth, and orientation of mineral crystals in the collagen matrix at different stages of mineralization. These findings will not only enable us to obtain a better understanding of the hierarchical structure of bone at the nanometer resolution, but also provide important design principles for hard tissue engineering and the development of biocompatible materials.

This work was supported by the DOE, BES (No. DE-FG02-06ER46276), and the NSF (No. DMR-0520894). We thank H. Wang, L. Graham, and M. J. Glimcher for providing Alewife herring bone samples, which were supported by NIH Grant No. AG014701 and a Peabody Foundation grant to M. J. G. We also thank them for many stimulating discussions. Use of beam line (No. BL29XUL) at SPring-8 was supported by RIKEN.

---

*miao@physics.ucla.edu

[1] S. W. White, D. J. S. Hulmes, A. Miller, and P. A. Timmins, Nature (London) **266**, 421 (1977).

[2] P. Fratzl, S. Schreiber, and A. Boyde, Calcif. Tissue Int. **58**, 341 (1996).

[3] H. E. Huxley and A. R. Faruqi, Annu Rev Biophys Bioeng **12**, 381 (1983).

[4] Y. Amemiya *et al.*, Science **237**, 164 (1987).

[5] D. J. Sege, A. L. Fink, K. O. Hodgson, and S. Doniach, Biochemistry **37**, 12 443 (1998).

[6] J. O. Rädler, I. Koltover, T. Salditt, and C. R. Safinya, Science **275**, 810 (1997).

[7] J. Miao, P. Charalambous, J. Kirz, and D. Sayre, Nature (London) **400**, 342 (1999).

[8] J. Miao *et al.*, Phys. Rev. Lett. **89**, 088303 (2002).

[9] D. Shapiro *et al.*, Proc. Natl. Acad. Sci. U.S.A. **102**, 15 343 (2005).

[10] M. A. Pfeifer *et al.*, Nature (London) **442**, 63 (2006).

[11] H. N. Chapman *et al.*, Nature Phys. **2**, 839 (2006).

[12] J. Miao *et al.*, Annu. Rev. Biophys. Biomol. Struct. **33**, 157 (2004).

[13] H. M. Quiney *et al.*, Nature Phys. **2**, 101 (2006).

[14] J. Miao, D. Sayre, and H. N. Chapman, J. Opt. Soc. Am. A **15**, 1662 (1998).

[15] M. J. Glimcher, in *Metabolic Bone Disease*, edited by L. V. Avioli and S. M. Krane (Academic Press, San Diego, 1998).

[16] H. W. Zhou *et al.*, J. Appl. Crystallogr. **40**, s666 (2007).

[17] W. Tong *et al.*, Calcif. Tissue Int. **72**, 592 (2003).

[18] A. J. Hodge, Connect. Tissue Res. **21**, 137 (1989).

[19] H. M. Kim, C. Rey, and M. J. Glimcher, J. Bone Miner. Res. **10**, 1589 (1995).

[20] Tamasaku *et al.*, Nucl. Instrum. Methods Phys. Res., Sect. A **467–468**, 686 (2001).

[21] J. Miao *et al.*, Phys. Rev. Lett. **95**, 085503 (2005).

[22] J. Miao *et al.*, Phys. Rev. Lett. **97**, 215503 (2006).

[23] C. C. Chen, J. Miao, C. W. Wang, and T. K. Lee, Phys. Rev. B **76**, 064113 (2007).

[24] See EPAPS Document No. E-PRLTAO-100-022803 for supplementary material. For more information on EPAPS, see http://www.aip.org/pubservs/epaps.html.

[25] H. D. Jiang and X. Y. Liu, J. Biol. Chem. **279**, 41 286 (2004).

[26] W. Zhang, S. S. Liao, and F. Z. Cui, Chem. Mater. **15**, 3221 (2003).

[27] M. J. Buehler, Nanotechnology **18**, 295102 (2007).

[28] H. Gao *et al.*, Proc. Natl. Acad. Sci. U.S.A. **100**, 5597 (2003).